

# INCORPORATING BOUNDARY UNCERTAINTY INTO LOSS FUNCTIONS FOR BIOMEDICAL IMAGE SEGMENTATION

*Michael Yeung<sup>1,2,3</sup>, Guang Yang<sup>3</sup>, Evis Sala<sup>2,4</sup>, Carola-Bibiane Schönlieb<sup>5</sup>, Leonardo Rundo<sup>2,4</sup>*

<sup>1</sup> School of Clinical Medicine, University of Cambridge, Cambridge, UK

<sup>2</sup> Department of Radiology, University of Cambridge, Cambridge, UK

<sup>3</sup> National Heart & Lung Institute, Imperial College London, London, UK

<sup>4</sup> Cancer Research UK Cambridge Centre, University of Cambridge, Cambridge, UK

<sup>5</sup> Department of Applied Mathematics and Theoretical Physics, University of Cambridge, Cambridge, UK

## ABSTRACT

Manual segmentation is used as the gold-standard for evaluating neural networks on automated image segmentation tasks. Due to considerable heterogeneity in shapes, colours and textures, demarcating object boundaries is particularly difficult in biomedical images, resulting in significant inter and intra-rater variability. Approaches, such as soft labelling and distance penalty term, apply a global transformation to the ground truth, redefining the loss function with respect to uncertainty. However, global operations are computationally expensive, and neither approach accurately reflects the uncertainty underlying manual annotation. In this paper, we propose the Boundary Uncertainty, which uses morphological operations to restrict soft labelling to object boundaries, providing an appropriate representation of uncertainty in ground truth labels, and may be adapted to enable robust model training where systematic manual segmentation errors are present. We incorporate Boundary Uncertainty with the Dice loss, achieving consistently improved performance across three well-validated biomedical imaging datasets compared to soft labelling and distance-weighted penalty. Boundary Uncertainty not only more accurately reflects the segmentation process, but it is also efficient, robust to segmentation errors and exhibits better generalisation.

**Index Terms**— Biomedical imaging, Image segmentation, Machine learning, Cost function

## 1. INTRODUCTION

Manual segmentation of biomedical images is performed by humans, often requiring expert knowledge, to assign each pixel of an image to a class. Not only is this process time-consuming, but the difficult, and often subjective nature, results in significant inter and intra-rater variability [1]. Automatic methods for biomedical image segmentation aim to address these issues, using manual segmentations to provide labels for supervised training and performance evaluations.

However, categorical labels from manual segmentation fail to capture the uncertainty associated with the process of humans assigning class labels.

A common approach in classification tasks to represent uncertainty is to apply soft labels (SLs) to the ground truth, converting binary decisions into probabilistic scores [2, 3]. Segmentation describes a pixel-wise classification task, and the equivalent therefore involves assigning soft labels to each pixel [4]. However, this form of global uncertainty ignores important spatial information, and is different from uncertainty in manual segmentation which is instead concentrated around class boundaries [5].

To focus optimisation on boundaries, the distance penalty term (DPT) computes Distance Transform Maps (DTMs) based on Euclidean distances to penalise predictions relative to class boundaries [6, 7]. However, generating DTMs are not only computationally expensive, but also increases the risk of overfitting by focusing too strictly on classifying boundary pixels according to the ground truth despite the uncertainty.

The main contributions of this work can be summarised as follows:

1. We propose a new ground truth transformation, known as Boundary Uncertainty (BU), which uses morphological operations to restrict soft labelling to boundary regions, providing an efficient approximation to segmentation uncertainty.
2. We demonstrate consistently improved performance with the balanced variant of BU across three well-validated datasets over SL and DPT.
3. We show the unbalanced variant of BU enables robust training when dealing with over-segmented and under-segmented labels.

## 2. MATERIALS AND METHODS

Boundary Uncertainty combines soft labelling with morphological operations to approximate segmentation uncertainty. Here, we first introduce soft labelling, followed by morpho-

logical operations, before describing Boundary Uncertainty, and conclude with dataset and implementation details. For all experiments, we use the original 2D U-Net as our baseline model, and apply ground truth transformations to the Dice loss [8, 9, 10].

## 2.1. Soft labels

Manual segmentation involves assigning class labels to each pixel in an image. In a binary segmentation task using one-hot encoded softmax outputs, the value for a pixel,  $p$ , at location  $x$  in the ground truth is defined as:

$$p_x : \begin{cases} p = 1, & \text{if } x \in \mathcal{T} \\ p = 0, & \text{if } x \notin \mathcal{T} \end{cases}, \quad (1)$$

where  $\mathcal{T}$  is the segmentation target.

To represent uncertainty, SL involves converting class labels into probabilistic scores:

$$p_x : \begin{cases} p \leq 1, & \text{if } x \in \mathcal{T} \\ p \geq 0, & \text{if } x \notin \mathcal{T} \end{cases}, \quad (2)$$

subject to:

$$p_{x \notin \mathcal{T}} \leq p_{x \in \mathcal{T}}. \quad (3)$$

Greater confidence in classifying a pixel as the segmentation target or background is represented as values closer to 1 and 0, respectively. To approximate manual segmentation uncertainty, we restrict SL to boundary regions using morphological operations.

## 2.2. Morphological operations

Morphological operations involve non-linear, local transformations on region boundaries. The two basic morphological transformations are erosion and dilation, applied to binary images by querying with a structuring element at all positions. Let  $I$  represent the input grey-scale image of size  $m \times n$ . Dilation ( $\oplus$ ) and erosion ( $\ominus$ ) operations are defined as:

$$(I \oplus W)(x, y) = \max_{i \in S_1, j \in S_2} (I(x - i, y - j) + W(i, j)), \quad (4)$$

$$(I \ominus W)(x, y) = \min_{i \in S_1, j \in S_2} (I(x + i, y + j) - W(i, j)), \quad (5)$$

where  $W$  is the structuring element.

## 2.3. Boundary Uncertainty

BU assigns pixels with probabilistic scores around boundary regions:

$$p_{x \in \mathcal{T}} : \begin{cases} p = \alpha, & \text{if } p \in ((I \oplus W)_{n_{\text{iter}}} - I) \\ p = \beta, & \text{if } p \in (I - (I \ominus W)_{n_{\text{iter}}}) \end{cases}, \quad (6)$$

where  $n_{\text{iter}}$  denotes the number of iterations of the morphological operation, and  $\alpha$  and  $\beta$  are hyperparameters that determine the SL values directly exterior and interior to the boundary region respectively (Fig. 1). The balanced form is subject to the constraint that  $\alpha + \beta = 1$  and  $\alpha \geq \beta$ , used for when segmentation errors are equally likely to occur either side of the boundary. The setting  $\alpha = 1$  and  $\beta = 0$  corresponds to the original hard labels.

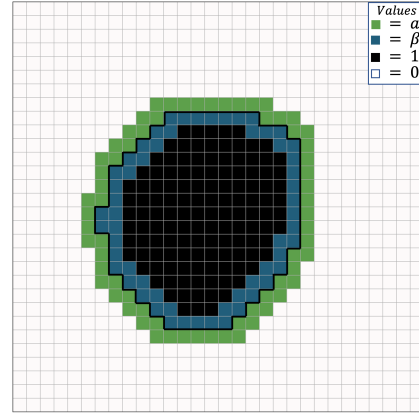


**Fig. 1.** Example of applying BU to a manual segmentation. The black border delineates the original manual segmentation. Morphological dilation expands the segmentation target into the green region, where values are assigned  $\alpha$ . In contrast, morphological erosion subtracts the blue region, where values are assigned  $\beta$ . Due to the local nature of morphological operations, all other pixels remain unaffected.

In contrast, the unbalanced form restricts  $0 \leq \alpha + \beta \leq 2$  and  $\alpha \geq \beta$ , used when there is systematic bias towards under-estimation or over-estimation of the segmentation target. The unbalanced form has been applied in highly class imbalanced segmentation, where dilation of the segmentation target improves recall with small segmentation targets [11, 12].

$n_{\text{iter}}$  determines the extent of BU, with larger values of  $n$  corresponding to larger regions of uncertainty.

In summary, BU enables robust model training by approximating segmentation error, which is mainly concentrated around boundaries, regardless of whether the errors are random or systematic in origin. The effect of different ground truth transformations are shown in Fig. 2.

## 2.4. Dataset descriptions and evaluation metrics

To evaluate BU, we select three well-validated, open-source biomedical imaging datasets, namely: Digital Retinal Images for Vessel Extraction (DRIVE), 2018 Data Science Bowl

**Table 1.** Hyperparameter tuning of BU on the DRIVE, 2018DSB and CVC-ClinicDB datasets. The highest scores are denoted in bold.

Hyperparameters		DRIVE			2018DSB			CVC-ClinicDB		
Alpha	Beta	DSC	Precision	Recall	DSC	Precision	Recall	DSC	Precision	Recall
1	0	0.8082	<b>0.8473</b>	0.7766	0.9147	<b>0.9205</b>	0.9168	0.8826	0.9175	0.8759
0.9	0.1	<b>0.8141</b>	0.8115	0.8211	<b>0.9171</b>	0.9139	0.9281	0.8928	0.9211	0.8844
0.8	0.2	0.8099	0.7870	0.8386	0.9162	0.9129	0.9268	0.8903	0.9146	<b>0.8892</b>
0.7	0.3	0.8025	0.7542	0.8621	0.9119	0.8952	0.9374	0.8787	0.8985	0.8811
0.6	0.4	0.7838	0.6759	0.8829	0.9043	0.8873	0.9319	<b>0.8962</b>	<b>0.9229</b>	0.8856
0.5	0.5	0.7347	0.6158	<b>0.9156</b>	0.8742	0.8197	<b>0.9500</b>	0.8903	0.9143	0.8874

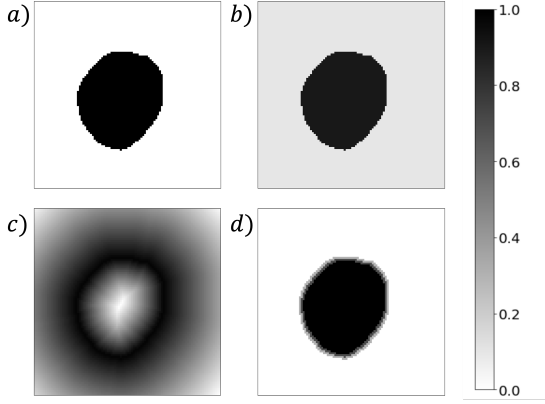


**Fig. 2.** Ground truth transformations where a) ground truth, b) SL, c) DPT and d) BU with  $\alpha = 0.7, \beta = 0.3$  and  $n = 1$ .

(2018DSB) and CVC-ClinicDB [13, 14, 15]. The DRIVE dataset contains 40 coloured fundus photographs used for retinal vessel segmentation, 2018DSB consists of 670 light microscopy images for nuclei segmentation, and the CVC-ClinicDB dataset consists of 612 frames of colorectal polyps obtained during optical colonoscopy. A summary of the datasets and training details are presented in Table 2.

**Table 2.** Details of datasets and training setup used for our experiments.

Dataset	Segmentation	#Images	Size	#Training	#Validation	#Test
DRIVE	Retinal vessel	40	512 × 512	16	4	20
2018DSB	Cell nuclei	670	256 × 256	428	108	134
CVC-ClinicDB	Colorectal polyp	612	288 × 384	392	98	122

For evaluation, we calculate Dice Similarity Coefficient (DSC), precision and recall metrics per image and average over the hold-out test set.

## 2.5. Implementation details

For our experiments, we used the Medical Image Segmentation with Convolutional Neural Networks (MIScnn) open-source Python library [16]. All experiments made use of Keras with Tensorflow backend, run on NVIDIA P100 GPUs. For all experiments, except for the DRIVE dataset which is already divided into 20 training images and 20 testing images, we randomly partitioned each dataset into 80% development

and 20% test set, with further division of the development set into 80% training set and 20% validation set. We used the following data augmentation: scaling, rotation, mirroring, elastic deformation and brightness. All images were normalised to  $[0, 1]$  using the z-score.

Model parameters were initialised using the Xavier initialisation. We trained each model with instance normalisation [17], using the Adam optimizer with a batch size of 1 and initial learning rate of  $1 \times 10^{-3}$ , and used ReduceLROnPlateau to reduce the learning rate by 0.1 if the validation loss did not improve after 25 epochs. The EarlyStopping callback was used to terminate training if the validation loss did not improve after 50 epochs.

SLs are set to 0.9 for the segmentation target and 0.1 for the background [12]. For BU, a grid search was performed to select optimal  $\alpha$  and  $\beta$  values for each dataset. For this preliminary study, A  $3 \times 3$  square structuring element was used, and we set  $n = 1$ .

To simulate under-segmentation and over-segmentation, we use morphological erosion and dilation operations, respectively, on the manual segmentations in the training set. In these experiments we used the unbalanced form of BU, setting  $\alpha = 1$  and  $\beta = 1$  for under-segmentation, and  $\alpha = 0$  and  $\beta = 0$  for over-segmentation.

## 3. RESULTS

### 3.1. Hyperparameter tuning

The results for the hyperparameter tuning experiments are shown in Table 1. The highest DSC values were obtained with  $\alpha = 0.9, \beta = 0.1$  for the DRIVE and 2018DSB experiments with a score of 0.8141 and 0.9171 respectively, higher than 0.8082 and 0.9147 obtained without BU. For CVC-ClinicDB, the highest DSC values of 0.8962 was obtained with  $\alpha = 0.6, \beta = 0.4$ , compared to 0.8826 with the original DSC loss. The lower optimal  $\alpha$  value for the CVC-ClinicDB dataset correlates with the greater uncertainty associated with delineating colorectal polyp boundaries compared to retinal vessels and cell nuclei. The general increase in recall and decrease in precision with higher values of  $\alpha$ , despite using the balanced form, is a property of using the Dice loss, which is biased towards assignment of the under-represented class.

**Table 3.** Evaluating robustness of the Dice loss with and without BU to under-segmentation and over-segmentation. The highest scores are denoted in bold.

Segmentation	Loss	DRIVE			2018DSB			CVC-ClinicDB		
		DSC	Precision	Recall	DSC	Precision	Recall	DSC	Precision	Recall
Under	DSC	0.4387	<b>0.9845</b>	0.2830	0.8040	<b>0.9653</b>	0.7034	0.8909	<b>0.9433</b>	0.8602
	DSC + BU	<b>0.7198</b>	0.8797	<b>0.6120</b>	<b>0.9130</b>	0.9231	<b>0.9107</b>	<b>0.8940</b>	0.9225	<b>0.8857</b>
Over	DSC	0.6730	0.5236	<b>0.9471</b>	0.8417	0.7514	<b>0.9709</b>	0.8742	0.8773	<b>0.9006</b>
	DSC + BU	<b>0.8093</b>	<b>0.8286</b>	0.7949	<b>0.9160</b>	<b>0.9108</b>	0.9291	<b>0.8797</b>	<b>0.8975</b>	0.8888

**Table 4.** Performance comparisons using different ground truth transformations on the DRIVE, 2018DSB and CVC-ClinicDB datasets. The highest scores are denoted in bold.

Loss	DRIVE			2018DSB			CVC-ClinicDB		
	DSC	Precision	Recall	DSC	Precision	Recall	DSC	Precision	Recall
DSC	0.8082	0.8473	0.7766	0.9147	0.9205	0.9168	0.8826	0.9175	0.8759
DSC + SL	0.8032	0.7420	<b>0.8797</b>	0.8863	0.8478	<b>0.9531</b>	0.8660	0.8417	<b>0.9267</b>
DSC + DPT	0.8086	<b>0.8498</b>	0.7751	0.9016	<b>0.9230</b>	0.8891	0.8174	0.9058	0.7614
DSC + BU	<b>0.8141</b>	0.8115	0.8211	<b>0.9171</b>	0.9139	0.9281	<b>0.8962</b>	<b>0.9229</b>	0.8856

### 3.2. Robustness to systematic segmentation error

The results for evaluating robustness to under-segmentation and over-segmentation are shown in Table 3. Including BU is associated with the highest DSC values across datasets for both under-segmentation and over-segmentation. The difference was most apparent in the DRIVE dataset, where the DSC score reduced to 0.4387 with under-segmented ground truth labels without BU, while only reduced to 0.7198 with BU. The smallest differences were observed with the CVC-ClinicDB, which as previous mentioned, may be due to the greater uncertainty associated with demarcating polyp boundaries.

### 3.3. Performance comparisons using different ground truth transformations

The results for different ground truth transformations are shown in Table 4. The highest DSC scores were consistently observed with BU. Using SL and DPT generally negatively affected the DSC score. By applying SL globally, the label noise generated by regions distant to the boundary may prevent optimal convergence. In contrast, DPT may attend to boundary regions too strictly, resulting in overfitting.

Example segmentations are shown in Fig. 3. Segmentations produced using BU are the most similar to the ground truth, even with difficult segmentations such as the CVC-ClinicDB example.

### 3.4. Efficiency comparisons of different ground truth transformations

Although ground truth transformations may be pre-computed prior to training, this is not possible when on-the-fly data augmentation is used. The training times using different ground truth transformations are shown in Fig. 4. Only DPT was associated with an increase in training time, demonstrating the efficiency of BU.

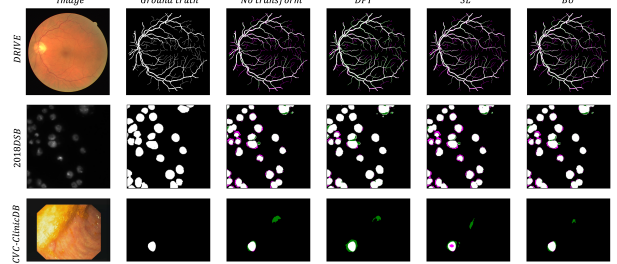


**Fig. 3.** Example segmentations using each ground truth transformation for the three datasets. False positive and false negative predictions are highlighted in green and purple, respectively.

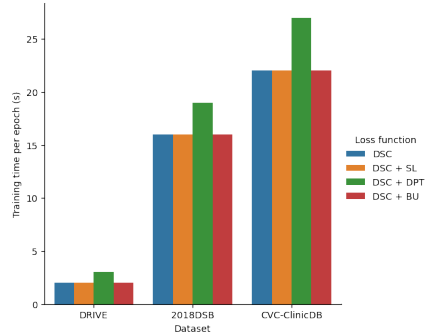


**Fig. 4.** Efficiency comparisons of different ground truth transformations on the DRIVE, 2018DSB and CVC-ClinicDB datasets.

## 4. CONCLUSION

In this work, we developed a new ground truth transformation, known as BU, to reflect segmentation uncertainty, by using morphological operations to restrict SL to boundary regions. We demonstrated improved performance using BU over global SL and DPT, across three well-validated biomedical imaging datasets. Moreover, we showed how BU may be adapted to provide robustness to over and under-segmentation. Finally, we confirmed that BU is an efficient operation, with no increase in training time. Appreciating the underlying uncertainty with manual segmentations not only more accurately reflects the nature of manual segmentation with biomedical images, but may also improve model generalisation to unseen datasets by reducing overfitting.

## 5. COMPLIANCE WITH ETHICAL STANDARDS

This research study was conducted retrospectively using open-source medical imaging datasets. Ethical approval was not required as confirmed by the license attached with the open access data.

## 6. REFERENCES

- [1] Simon K Warfield, Kelly H Zou, and William M Wells, “Simultaneous truth and performance level estimation (STAPLE): an algorithm for the validation of image segmentation,” *IEEE Trans. Med. Imaging*, vol. 23, no. 7, pp. 903–921, 2004.
- [2] Quang Nguyen, Hamed Valizadegan, and Milos Hauskrecht, “Learning classification models with soft-label information,” *Journal of the American Medical Informatics Association*, vol. 21, no. 3, pp. 501–508, 2014.
- [3] Christian Szegedy, Vincent Vanhoucke, Sergey Ioffe, Jon Shlens, and Zbigniew Wojna, “Rethinking the inception architecture for computer vision,” in *Proc. IEEE Conference on Computer Vision and Pattern Recognition*, 2016, pp. 2818–2826.
- [4] Lu Wang, Chaoli Wang, Zhanquan Sun, and Sheng Chen, “An improved dice loss for pneumothorax segmentation by mining the information of negative areas,” *IEEE Access*, vol. 8, pp. 167939–167949, 2020.
- [5] Michael C Krygier, Tyler LaBonte, Carianne Martinez, Chance Norris, Krish Sharma, Lincoln N Collins, Partha P Mukherjee, and Scott A Roberts, “Quantifying the unknown impact of segmentation uncertainty on image-based simulations,” *Nature Communications*, vol. 12, no. 1, pp. 1–11, 2021.
- [6] Hoel Kervadec, Jihene Bouchtiba, Christian Desrosiers, Eric Granger, Jose Dolz, and Ismail Ben Ayed, “Boundary loss for highly unbalanced segmentation,” in *Proc. International Conference on Medical Imaging with Deep Learning (MIDL)*. PMLR, 2019, pp. 285–296.
- [7] Takaaki Sugino, Toshihiro Kawase, Shinya Onogi, Taichi Kin, Nobuhito Saito, and Yoshikazu Nakajima, “Loss weightings for improving imbalanced brain structure segmentation using fully convolutional networks,” in *Healthcare*. Multidisciplinary Digital Publishing Institute, 2021, vol. 9, p. 938.
- [8] Olaf Ronneberger, Philipp Fischer, and Thomas Brox, “U-Net: Convolutional networks for biomedical image segmentation,” in *Proc. International Conference on Medical Image Computing and Computer-Assisted Intervention (MICCAI)*. Springer, 2015, pp. 234–241.
- [9] Fausto Milletari, Nassir Navab, and Seyed-Ahmad Ahmadi, “V-net: Fully convolutional neural networks for volumetric medical image segmentation,” in *2016 fourth international conference on 3D vision (3DV)*. IEEE, 2016, pp. 565–571.
- [10] Michael Yeung, Evis Sala, Carola-Bibiane Schönlieb, and Leonardo Rundo, “Unified focal loss: Generalising dice and cross entropy-based losses to handle class imbalanced medical image segmentation,” *arXiv preprint arXiv:2102.04525*, 2021.
- [11] Xianzhi Du, Xiaolong Wang, Dawei Li, Jingwen Zhu, Serafettin Tasçi, Cameron Upright, Stephen Walsh, and Larry Davis, “Boundary-sensitive network for portrait segmentation,” in *2019 14th IEEE International Conference on Automatic Face & Gesture Recognition (FG 2019)*. IEEE, 2019, pp. 1–8.
- [12] Pei Wang and Albert CS Chung, “Focal dice loss and image dilation for brain tumor segmentation,” in *Deep Learning in Medical Image Analysis and Multimodal Learning for Clinical Decision Support*, pp. 119–127. Springer, 2018.
- [13] Joes Staal, Michael D Abràmoff, Meindert Niemeijer, Max A Viergever, and Bram Van Ginneken, “Ridge-based vessel segmentation in color images of the retina,” *IEEE Trans. Med. Imaging*, vol. 23, no. 4, pp. 501–509, 2004.
- [14] Juan C Caicedo, Allen Goodman, Kyle W Karhohs, Beth A Cimini, Jeanelle Ackerman, Marzieh Haghighi, CherKeng Heng, Tim Becker, Minh Doan, Claire McQuin, et al., “Nucleus segmentation across imaging experiments: the 2018 data science bowl,” *Nature Methods*, vol. 16, no. 12, pp. 1247–1253, 2019.
- [15] Jorge Bernal, F Javier Sánchez, Gloria Fernández-Esparrach, Debora Gil, Cristina Rodríguez, and Fernando Vilariño, “WM-DOVA maps for accurate polyp highlighting in colonoscopy: Validation vs. saliency maps from physicians,” *Comput. Med. Imaging Graph.*, vol. 43, pp. 99–111, 2015.
- [16] Dominik Müller and Frank Kramer, “MIScnn: a framework for medical image segmentation with convolutional neural networks and deep learning,” *BMC Med. Imaging*, vol. 21, no. 1, pp. 1–11, 2021.
- [17] Xiao-Yun Zhou and Guang-Zhong Yang, “Normalization in training U-Net for 2-D biomedical semantic segmentation,” *IEEE Robotics and Automation Letters*, vol. 4, no. 2, pp. 1792–1799, 2019.